

1 Intrinsic neural timescales in the temporal
2 lobe support an auditory processing hierarchy

3

4 Riccardo Cusinato^{1,2,*}, Sigurd L. Alnes^{1,2,*}, Ellen van Maren², Ida Boccalaro², Debora
5 Ledergerber³, Antoine Adamantidis², Lukas L. Imbach³, Kaspar Schindler², Maxime O. Baud²,
6 Athina Tzovara^{1,2,4,#}

7

8 *1 Institute of Computer Science, University of Bern, Switzerland;*

9 *2 Center for Experimental Neurology - Sleep Wake Epilepsy Center - NeuroTec, Department of*
10 *Neurology, Inselspital, Bern University Hospital, University of Bern, Switzerland;*

11 *3 Swiss Epilepsy Center, Klinik Lengg, Zurich, Switzerland;*

12 *4 Helen Wills Neuroscience Institute, University of California Berkeley, USA*

13

14 ** These authors contributed equally to this work*

15 *# Corresponding author: athina.tz@gmail.com*

16 Abstract

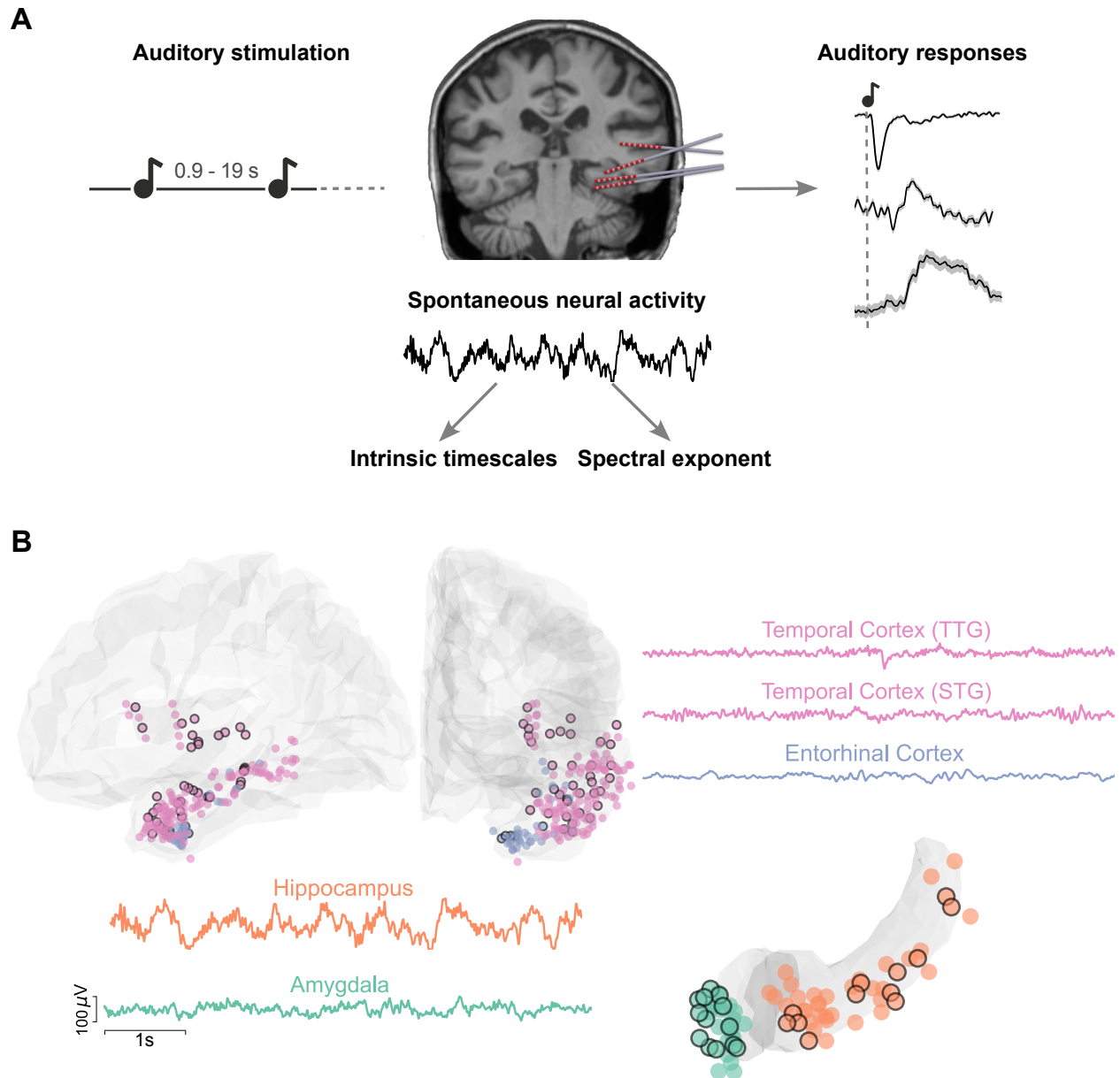
17 During rest, intrinsic neural dynamics manifest at multiple timescales, which progressively
18 increase along visual and somatosensory hierarchies. Theoretically, intrinsic timescales are
19 thought to facilitate processing of external stimuli at multiple stages. However, direct links
20 between timescales at rest and sensory processing, as well as translation to the auditory system
21 are lacking. Here, we used intracranial electroencephalography in humans to show that in the
22 auditory network, intrinsic neural timescales progressively increase, while the spectral slope
23 flattens, from temporal to entorhinal cortex, hippocampus, and amygdala. Within the neocortex,
24 intrinsic timescales exhibit spatial gradients that follow the temporal lobe anatomy. Crucially,
25 intrinsic timescales at rest can explain the latency of auditory responses: as intrinsic timescales
26 increase, so do the single-electrode response onset and peak latencies. Our results suggest that
27 the human auditory network exhibits a repertoire of intrinsic neural dynamics, which manifest in
28 cortical gradients with millimeter resolution and may provide a variety of temporal windows to
29 support auditory processing.

30 Introduction

31 The human brain gives rise to rich neural dynamics that mediate perception and cognition, and
32 operate at multiple timescales (Honey et al., 2012; Murray et al., 2014). In the visual and
33 somatosensory systems, intrinsic timescales manifest at rest, in ongoing neural activity: primary
34 areas exhibit short timescales that may facilitate a quick reaction to incoming stimuli (Gao et al.,
35 2020; Murray et al., 2014; Raut et al., 2020). These progressively increase while advancing
36 through the cortical hierarchy, likely supporting integration of information (Chaudhuri et al., 2015;
37 Murray et al., 2014). Whether a similar hierarchy of intrinsic dynamics exists in the temporal lobe,
38 a hub for auditory processing, remains unknown.

39 In the auditory system, evidence for processing of external stimuli at multiple latencies stems from
40 studying evoked responses. Primary auditory areas typically show fast and short-lasting
41 responses, which may progressively increase while advancing to secondary areas (Camalier et
42 al., 2012, Nourski et al., 2014). Beyond this ‘classical’ circuitry, an extensive network of adjacent
43 regions is also sensitive to auditory input. These exhibit diverse response profiles and latencies,
44 and include, for instance, the insula (Blenkmann et al., 2019), or the hippocampus and amygdala,
45 which show slower, long-lasting responses to sounds (Halgren et al., 1980). Despite this diversity
46 in auditory response profiles, a detailed characterization of temporal lobe dynamics at rest and
47 their contribution to auditory processing remains an open question. In humans, in particular, a
48 fine-grained measurement of neural dynamics in the temporal lobe can be challenging with non-
49 invasive techniques (Tzovara et al., 2019), but evidence from invasive recordings remains limited.

50 Here, we hypothesized that intrinsic neural timescales at rest, estimated by characteristic
51 latencies of the autocorrelation function (ACF) of intracranial electroencephalography (iEEG)
52 signals, would show a hierarchical organization within an extended auditory network, which could,
53 in turn, explain a hierarchy of neural responses to incoming auditory stimuli. We additionally
54 hypothesized that non-oscillatory brain dynamics, characterized by the spectral exponent of
55 aperiodic neural activity, which has been suggested to be a proxy of the excitation to inhibition
56 balance (Gao et al., 2017), would also reveal a hierarchical organization across the temporal lobe.



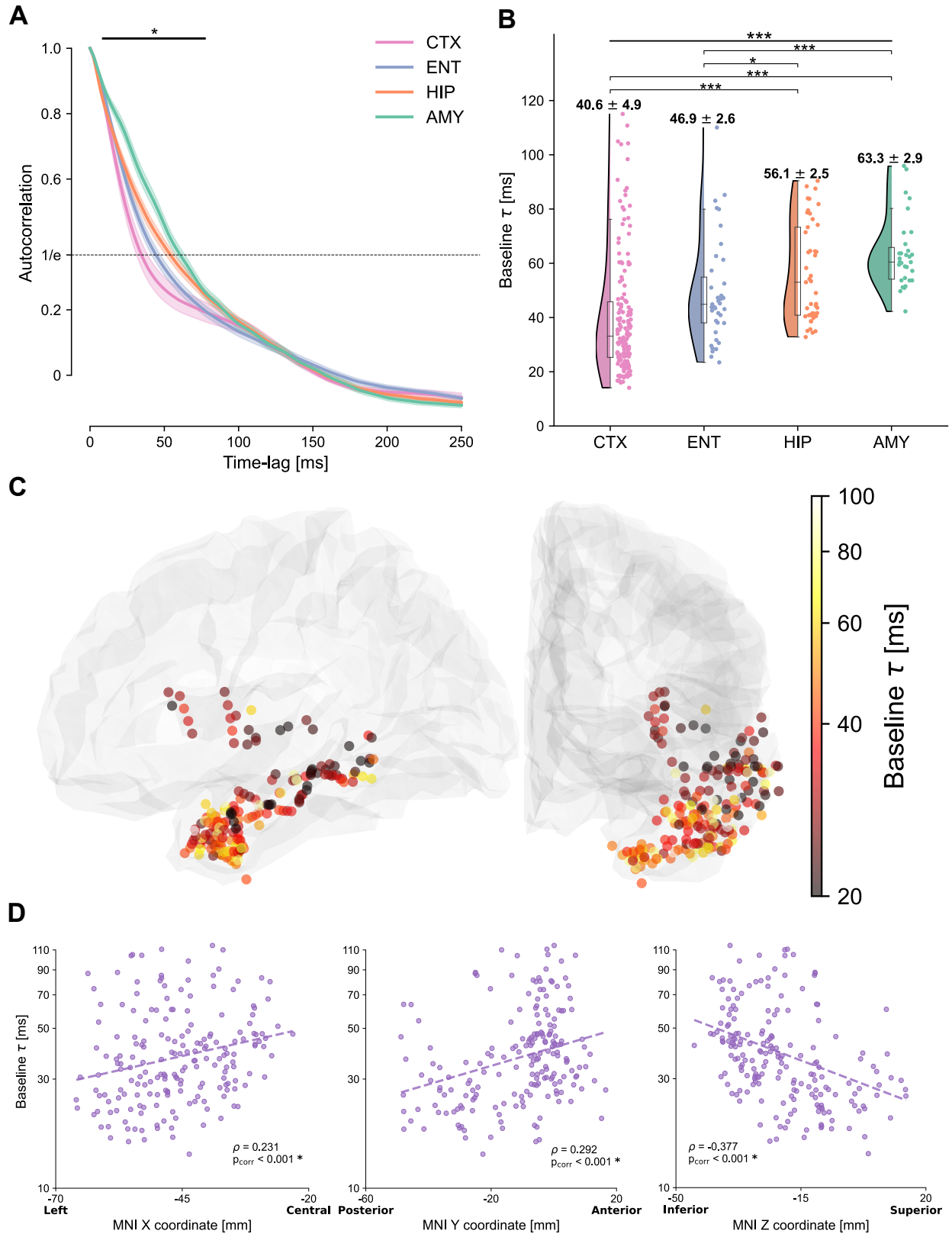
57

Figure 1. Experimental paradigm, electrode coverage, and exemplar iEEG traces. A. Summary of the main analyses and methodology. Left: schematic of the auditory stimulation protocol: Patients were presented with 100 ms pure tones, occurring at random intervals between 0.9-19 s. Middle: Example of implanted iEEG electrodes and exemplar raw trace of spontaneous neural activity from one electrode, before sound presentation, which is used to estimate intrinsic timescales and spectral exponents. Right: intracranial event-related potentials (iERPs) are extracted in response to the sounds. These are displayed for a schematic illustration of our protocol, for three exemplar electrodes, and are presented in more detail in Figure 3. B. Illustration of recorded electrodes (N=270) over the group of 11 patients. Black-circled electrodes are responsive to the auditory stimulation. As exemplar signals, we show iEEG traces from the transverse and superior temporal gyri (TTG and STG, pink), the entorhinal cortex (light blue), hippocampus (orange), and amygdala (green). Each of these regions exhibits characteristic and distinct dynamics at rest, displayed here over a 6 s segment.

71 Results

72 We recorded iEEG in 270 electrodes from 11 patients with epilepsy, undergoing pre-surgical
73 monitoring, presented with pure tones at random intervals (Figure 1A, Suppl. Table 1). Initially,
74 we assessed a macroscopic organization of neural dynamics by dividing iEEG signals into regions
75 of interest, selected based on the most consistent implantations across patients, targeting the
76 entorhinal cortex (ENT), hippocampus (HIP), and amygdala (AMY) with their innermost
77 electrodes, with additional electrodes covering the temporal and adjacent cortices (CTX) (Figure
78 1B, Supplemental Material for sub-divisions of cortical electrodes). Subsequently, we grouped all
79 available electrodes together and assessed their spatial organization at a finer level, with respect
80 to cortical and subcortical anatomies.

81 We computed the autocorrelation function of baseline iEEG, which quantifies how similar a time
82 series is to its past values across multiple time lags. The mean autocorrelation across brain
83 regions shows a characteristic decay (Figure 2A) and for short time lags follows an ordering:
84 electrodes in the temporal cortex have the most rapid decay, followed by electrodes in the
85 entorhinal cortex, the hippocampus, and last, amygdala (Figure 2A, significant main effect of
86 region for time-lags between 10 and 80 ms, $p_{\text{corr}} < 0.05$).



87

88 **Figure 2. Autocorrelation function and intrinsic neural timescales at rest.** A. Average
89 autocorrelation function across electrodes and patients, for electrodes in the temporal (pink) and

90 entorhinal (light blue) cortices, hippocampus (orange), and amygdala (green). The autocorrelation
91 shows a significant main effect of region for time lags between 10 and 80 ms (horizontal solid
92 bar). The dashed horizontal line at $1/e$ (inverse of natural logarithm) displays the value of the
93 autocorrelation for which the characteristic timescales are extracted. B. Intrinsic timescales at
94 baseline (τ), plotted for each electrode, show a main effect of region, with significantly faster
95 timescales for the temporal and entorhinal cortices compared to the hippocampus and amygdala.
96 C. The spatial organization of intrinsic timescales follows the cortical anatomy. Electrodes in the
97 posterior/superior temporal cortex exhibit the fastest timescales, which progressively increase
98 along the anterior/inferior axis. The color map quantifies the intrinsic timescale for each electrode
99 on a logarithmic scale. For display purposes, all electrodes have been projected to the left
100 hemisphere. D. Gradients of timescales spanning the cortex, plotted as timescales along the X,
101 Y, and Z MNI coordinates of each electrode. Timescales significantly correlate with MNI
102 coordinates in all three dimensions, tracking the cortical anatomy.

103

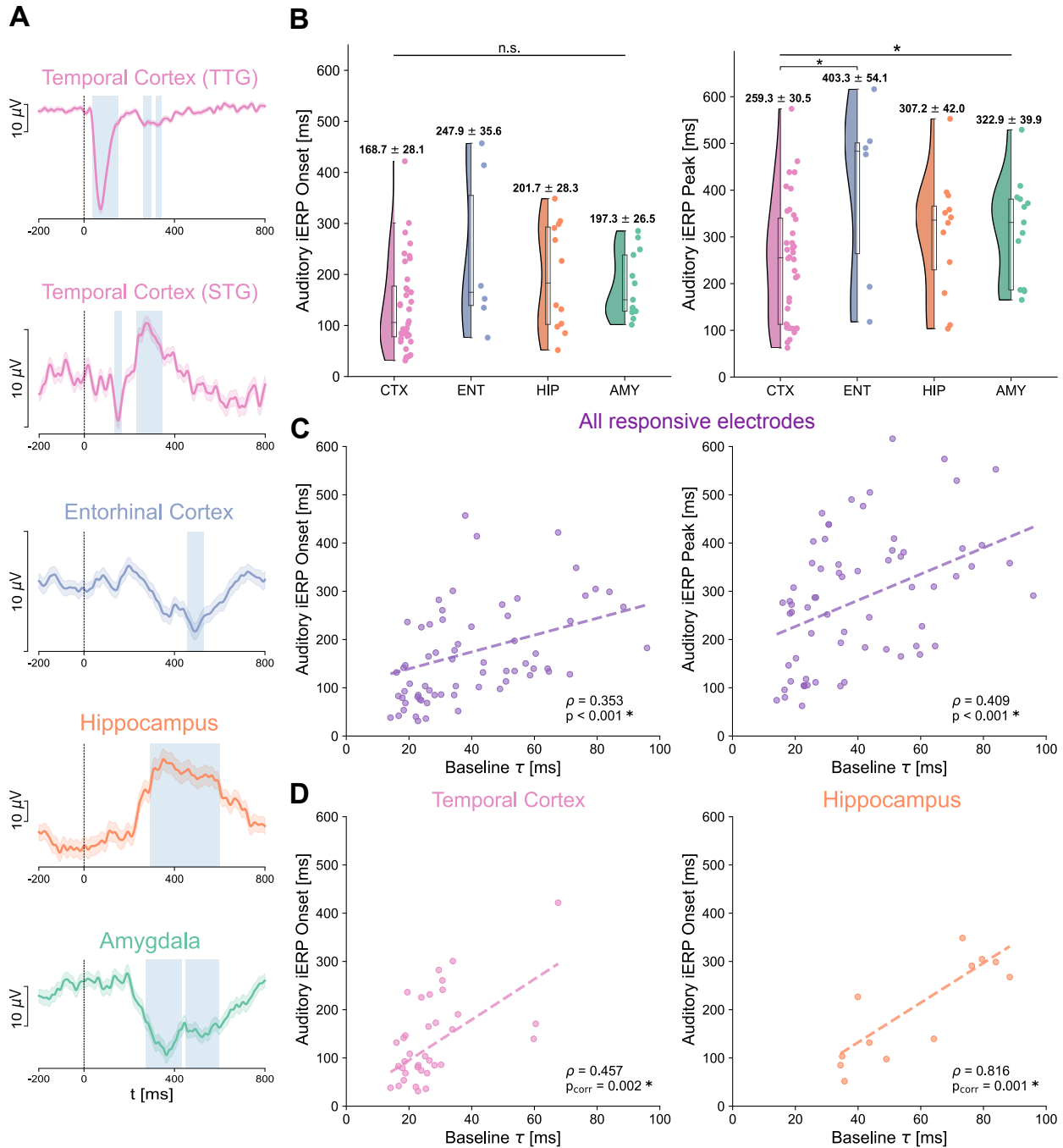
104 We then computed intrinsic neural timescales (τ), defined as the time lag at which the
105 autocorrelation decays to a fixed threshold. Intrinsic timescales show a significant main effect of
106 brain region ($F(3,256)=27.313$, $p<10^{-14}$, mixed-effects model) (Figure 2B), and reveal a
107 macroscopic hierarchy at rest: the temporal cortex exhibits significantly faster intrinsic timescales,
108 compared to both hippocampus and amygdala (Suppl. Table 2). Within subregions of the cortex,
109 intrinsic timescales tend to be slower in the pole, and faster in the transverse gyrus, while the
110 superior, middle and inferior temporal cortex or the insula lie in between (Suppl. Figure 2-1). The
111 entorhinal cortex is also significantly faster compared to other limbic areas, but not different from
112 the temporal cortex (Suppl. Table 1).

113 At a finer scale, within the temporal and entorhinal cortices, intrinsic timescales at rest show a
114 gradient that spans the temporal lobe through the postero-lateral (fast timescales) to the antero-
115 medial (slow timescales) axis (Figure 2C). This gradient is particularly prominent in the Y and Z
116 directions that primarily define the temporal lobe orientation (Figure 2D, $\rho_x=0.231$, $p_x<10^{-5}$;
117 $\rho_y=0.292$, $p_y<10^{-8}$; $\rho_z=-0.377$, $p_z<10^{-11}$, accounting for inter-subject variability and Bonferroni
118 corrected). The spatial distribution of timescales in the hippocampus and amygdala is by contrast
119 less defined (Suppl. Figure 2-2).

120 We next investigated whether intrinsic timescales at rest could explain the timing of auditory
121 processing. iERPs across brain regions show striking qualitative differences in terms of amplitude
122 and response timing (Figure 3A). To quantify these diverse auditory response profiles, we
123 computed the response onset and peak latencies of electrodes showing a significant 1-40 Hz
124 auditory response (N=67 out of 270 total electrodes, Figure 3A/B). Cortical electrodes generally
125 show faster responses than hippocampal and amygdalar ones both for onset and peak, but at the

126 group level, there is no significant effect of region ($F(3,55)=1.867$, $p=0.146$; $F(3,55)=2.774$,
 127 $p=0.0499$ for onset/peak, Figure 3B and Suppl. Figure 3-1 for sub-regions).

128



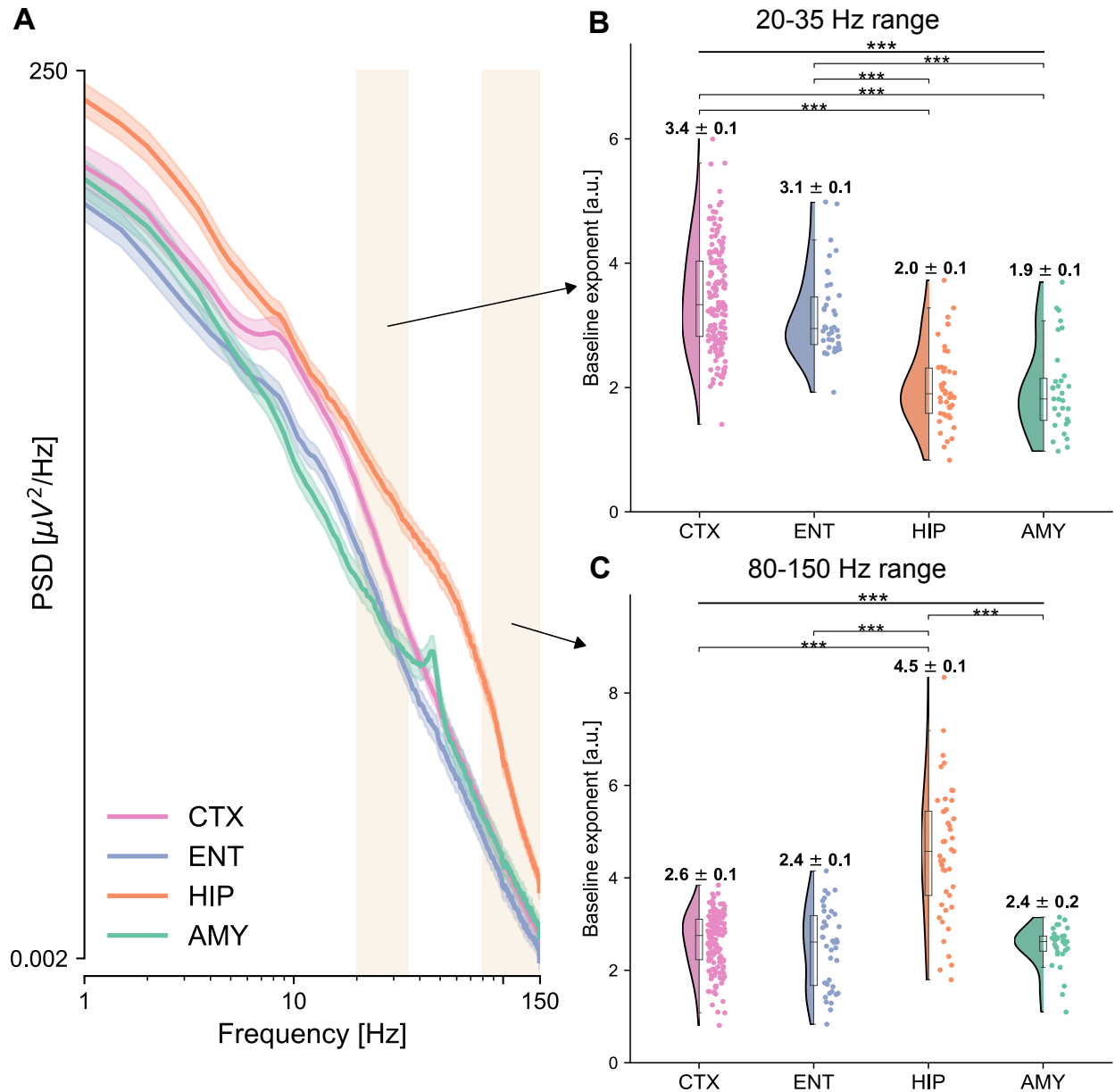
129

130 **Figure 3. Onset and peak latencies of auditory responses across brain regions and their**
 131 **relation to intrinsic timescales at rest. A.** Exemplar auditory responses for each of the recorded
 132 regions (1-40 Hz iERPs). Time 0 corresponds to sound onset. Auditory responses in the

133 transverse temporal gyrus (TTG) are the earliest, shorter-lasting, and exhibit the largest amplitude
134 (top plot). Responses in other cortical regions, e.g. the superior temporal gyrus (STG), have a
135 relatively early onset, and later peak, while responses in the entorhinal cortex, hippocampus, and
136 amygdala (third to fifth row) are typically smoother, long-lasting, and with later peaks. The
137 variability in response amplitudes is indicated by the different spans of a $10\mu\text{V}$ scale on the y-
138 axis. B. Auditory response onsets (left panel) and peaks (right panel) for all responsive electrodes.
139 The temporal cortex shows the earliest onset and peak across all brain regions, with responses
140 starting on average at 168.7 ms, and peaking at 259 ms post sound onset, followed by the
141 hippocampus/amygdala, and entorhinal cortex. C. Regression of intrinsic timescales τ at baseline
142 (x-axis) on auditory iERP onsets (y-axis, left panel) and peaks (y-axis, right panel) across all
143 responsive electrodes. Regression of intrinsic timescales on both onsets and peaks is highly
144 significant, accounting for across-patient variations, suggesting that intrinsic timescales can
145 explain the timing of auditory responses at the single electrode level. D. A significant regression
146 of characteristic timescales on iERP onsets also persists within the temporal cortex (left panel),
147 and hippocampus only (right panel), but not in the amygdala or entorhinal cortex (Suppl. Figure
148 3-2).

149

150 This variability in onset and peak latencies within and between brain regions can be partially
151 explained when accounting for differences in intrinsic timescales (Figure 3C). We computed a
152 regression of intrinsic timescales on response latencies, which shows a highly significant main
153 effect of timescale at baseline both on response onset ($p=0.353$, $p=0.0009$) and peak latencies
154 ($p=0.409$, $p=0.0005$). The significant regression on onset latency holds for electrodes within the
155 temporal cortex ($p=0.457$, $p_{\text{corr}}=0.0017$) and hippocampus ($p=0.816$, $p_{\text{corr}}=0.0013$, Figure 3D)
156 (Suppl Figure 3-2 for other sub-regions). These results suggest that regions characterized by fast
157 intrinsic timescales exhibit a fast reaction to incoming auditory stimuli, while the hippocampus,
158 amygdala, and entorhinal cortex are mediated by slower ongoing dynamics and slower auditory
159 responses.



160

161 **Figure 4. Power spectra and spectral exponents across brain regions.** A. Average power
162 spectra are displayed for the four regions of interest. Cortex (pink) exhibits a characteristic
163 oscillatory peak around 10 Hz, and a relatively fast decay, while the hippocampus (orange)
164 displays the strongest power, which for low frequencies decays relatively gently, but after 70 Hz
165 much faster. The shaded rectangles highlight the two frequency ranges for which the spectral
166 exponent is computed, at 20-35 Hz, and at 80-150 Hz. x- and y-axes are plotted in logarithmic
167 scales. B/C. Spectral exponent at 20-35 Hz (B) and 80-150 Hz (C), for each electrode and region
168 of interest. The spectral exponent in the 20-35 Hz range shows a significant main effect of region,
169 with the temporal cortex having the steepest exponent followed by the entorhinal cortex, the
170 hippocampus, and amygdala, which have flatter exponents. The 20-35 Hz exponent values for
171 cortical subdivisions can be found in Suppl Figure 4-1. The spectral exponent at 80-150 Hz also
172 shows a significant effect of region, with the hippocampus having the steepest exponent among

173 all other regions, compatible with the “knee” observed in the average power spectra (panel A).
174 The corresponding offsets for both ranges are reported in Suppl Figure 4-2.

175 To confirm the observed hierarchy of intrinsic neural dynamics, we additionally characterized the
176 non-oscillatory part of the power spectra by their spectral exponent (slope in log-log space) in the
177 ranges 20-35 and 80-150 Hz (Figure 4A). Electrodes in the temporal cortex have the steepest 20-
178 35 Hz exponent, followed by the entorhinal cortex, hippocampus, and amygdala (Figure 4B,
179 significant effect of region, $F(3,256)=80.665$, $p<10^{-16}$), confirming the ordering observed for
180 intrinsic timescales (Suppl. Table 3). The spectral exponent in the 80-150 Hz range also shows a
181 significant main effect of region ($F(3,256)=79.156$, $p<10^{-16}$, Figure 4C), mainly driven by the
182 difference between the hippocampus and all other regions (Suppl. Table 4). Similar to the intrinsic
183 timescales, the 20-35 Hz spectral exponent shows a significant, albeit weaker, correlation with
184 MNI X and Z coordinates (Suppl Figure 4-3 and Suppl Figure 4-4 for within
185 hippocampus/amygdala), providing further support for a gradient organization of neural dynamics
186 within the extended auditory cortical network.

187 Discussion

188 We provide evidence for a hierarchy of intrinsic neural dynamics in the extended human auditory
189 network at rest, which in turn explains a hierarchy in the processing of incoming auditory stimuli.
190 The temporal cortex assumes a “low” position along this hierarchy, highlighted by short intrinsic
191 timescales, which may mediate short temporal receptive windows (Hasson et al., 2008), and by
192 a steep 20-35 Hz spectral exponent, which may indicate a shift towards inhibitory activity (Gao et
193 al., 2017). On the contrary, the hippocampus and amygdala exhibit longer intrinsic timescales and
194 a flatter exponent, likely indicative of an integrative function (Golesorkhi et al., 2021; Murray et
195 al., 2014). Our findings are in line with previous reports of a hierarchical organization of intrinsic
196 timescales in the visual and somatosensory modalities, which progressively increase along the
197 cortical hierarchy (Murray et al., 2014), and also with reports of a hierarchical organization in
198 synaptic excitation (Wang, 2020). Although here we were not able to directly measure
199 excitation/inhibition, the steepness of the spectral exponent around the 20-35 Hz range has been
200 suggested to reflect the excitation to inhibition balance (Gao et al., 2017), or levels of neural
201 “noise” (Alnes et al., 2021). The particularly steep hippocampal spectral exponent for high
202 frequencies, by contrast, reflects the abrupt change of slope in the hippocampal power spectrum,
203 which forms a “knee” at around 70 Hz (Figure 4A).

204 We additionally show that the hierarchy of intrinsic neural dynamics of the extended auditory
205 network manifests as a continuous gradient along the anatomy of the temporal lobe, both for
206 intrinsic timescales and spectral exponents. We did not find evidence for gradients of timescales
207 within the hippocampus and amygdala, contrary to a recent magnetic resonance imaging study
208 (Raut et al., 2020), possibly because of a sparser coverage or because these may only manifest
209 at very slow dynamics.

210 Although several studies have posited that short intrinsic timescales may mediate fast responses
211 to incoming stimuli, we now provide direct evidence for the auditory modality. We show, in the
212 same patients and recordings, that the diversity of intrinsic timescales partially explains the
213 richness of auditory response onset and peak latencies. Although our analyses are correlational,
214 we posit that this repertoire of intrinsic timescales at rest may support the auditory process itself,
215 providing a variety of processing windows (Golesorkhi, et al., 2021). How this hierarchy supports
216 processing of more complex stimuli, or whether it expands to structures of the midbrain can be
217 the topic of future investigations.

218 In summary, our results show a hierarchy of neural dynamics in the extended human auditory
219 network that manifests across cortical and limbic structures, exhibits anatomical gradients with
220 millimeter resolution and can explain the temporal richness of neural responses to auditory stimuli.

221

222 Methods

223 Patients

224 We recorded intracranial EEG in 11 neurosurgical patients (4 women, median age=32 years,
225 min=27, max=56) with drug-refractory epilepsy who had been implanted with depth electrodes to
226 identify seizure foci (Supplemental Table 1 for a detailed patient description). Electrode locations
227 were based on clinical criteria only. Recordings took place at the EPI Clinic, Zurich, and at the
228 Inselspital, Bern. Patients provided written informed consent prior to participation in this research
229 study, approved by institutional ethics review boards of the Canton of Zurich (PB-2016-02055),
230 and Inselspital, Bern (# 2018-01387). All experiments were performed in accordance with the 6th
231 Declaration of Helsinki.

232 Experimental protocol

233 Patients were presented with auditory stimuli consisting of pure tones at three frequencies (500,
234 1250, 2500 Hz) with a random interstimulus interval between 0.9 and 19 seconds. Each tone had
235 a duration of 100 ms with 5 ms on/off ramps to avoid clicks. Interstimulus interval and tone
236 frequency were drawn from a pseudorandom distribution such that each was played 120 times
237 per hour (in total 360 tones per hour). Auditory stimuli were presented via in-ear headphones, and
238 their intensity was adjusted individually for each patient at a comfortable level. Patients were
239 instructed to relax and ignore the sounds. Some of the patients were additionally presented with
240 the auditory stimuli during sleep, at a later session, which was not analyzed in the context of the
241 present study.

242

243 iEEG recordings & preprocessing

244 Depth electrodes were used for iEEG recordings (DIXI Medical, 3 patients; Ad-Tech Medical, 8
245 patients) targeting different brain regions and varying from eight to eighteen platinum iEEG
246 contacts along their shaft. Data were recorded at 4096 or 1024 Hz. Recordings with 4096 Hz
247 sampling rate were downsampled offline to 1024 Hz.

248 All data were visually inspected to exclude electrodes with persistent spiking activity. Continuous
249 data were notch filtered around 50 Hz and harmonics, and re-referenced with a bipolar scheme,
250 i.e. each electrode to the closest one in the same electrode lead outwardly, to remove any source
251 of widespread noise. This was done to retain a local signal and mitigate effects of volume
252 conductance, following recommendations in the analysis of iEEG data (Lachaux et al., 2012;
253 Mercier et al., 2022). Peri-stimulus epochs were then extracted, spanning from -5 s before the
254 sounds' onset to 5 s post-stimulus onset. Only epochs that did not overlap with another sound in
255 this period were kept. All epochs were then visually inspected and any epochs with remaining
256 artifacts were rejected. The baseline period of each epoch was defined as the interval [-1,0] s
257 preceding the sounds. For studying auditory responses (see Responsive electrodes section), the
258 raw signal from all electrodes was additionally band-pass filtered between 1-40 Hz. Processing
259 of iEEG data was performed using MNE python (Gramfort et al., 2013).

260 Electrode localization

261 Electrodes were localized on post-implant computed tomography (CT) scans using the Lead-DBS
262 toolbox (Horn & Kühn, 2015) and transformed into standard MNI coordinates for group analyses.

263 The post-implant CT scan was registered to a pre-implant structural T1-weighted magnetic
264 resonance imaging (MRI) scan from which anatomical labels were reconstructed using the
265 FreeSurfer toolbox and the Destrieux atlas. Subsequently, electrode coordinates identified on the
266 post-implant CT scans were mapped to their corresponding anatomical regions identified on the
267 pre-implant MRI. Anatomical label assignment was validated for all electrodes by an expert
268 neurologist, who verified their location and additionally ensured that none of the electrodes that
269 were included in our analyses were in white matter. The available electrodes were divided across
270 four regions of interest, covering the temporal cortex, the insula due to its prominent auditory
271 responses, entorhinal cortex, hippocampus, and amygdala. This resulted in N=270 electrodes in
272 total, with a median=25, min=8 and max = 37 electrodes per patient.

273 Intrinsic neural timescales

274 For estimating intrinsic neural timescales, we first computed the Autocorrelation function (ACF)
275 on each epoch during 1 s baseline period (function *acf* from Python's statsmodels (Seabold &
276 Perktold, 2010)). The resulting ACFs across epochs were then averaged to yield a single ACF for
277 each electrode. Following previous literature (Chaudhuri et al., 2015; Gao et al., 2020; Golesorkhi,
278 et al., 2021; Murray et al., 2014), we then defined the "intrinsic timescale" of each electrode as
279 the time lag at which the ACF reaches the value $1/e$, consistent with an analytical decay of the
280 form $f(t)=\exp(-t/\tau)$. The precise time-lag was computed by interpolating with a spline fit to the ACF,
281 as in (Raut et al., 2020).

282 Power spectral density and spectral exponent

283 For estimating the spectral exponent, we computed power spectra with a Hann-windowed and
284 detrended Fourier transform on the baseline period (function *spectrogram* from Python's scipy
285 (Virtanen et al., 2020)). Power spectra were averaged using a "meanlog" approach, i.e. taking the
286 mean of the logarithm of the power spectrum across epochs, to yield a single power spectrum
287 density for each electrode.

288 The spectral exponent was then computed on each electrode's average power spectrum density
289 using the standard implementation of the spectral parameterization algorithm (Donoghue et al.,
290 2020) in the "fixed" mode (linear fit in log-log plot) in two different frequency ranges: a lower one,
291 at 20-35 Hz, and a higher one, at 80-150 Hz. The lower range was chosen following a large body
292 of literature in order to avoid low-frequency knees, high-power peaks and spectral plateaus, and

293 has been previously linked to excitation to inhibition balance (Gao et al., 2017; Gerster et al.,
294 2021; Lendner et al., 2020). The higher range was chosen as a typical high frequency range that
295 is often computed in iEEG studies, as a proxy to neuronal firing (Lachaux et al., 2012). The
296 spectral exponent was computed as the slope of non periodic parts of the power spectra observed
297 at each electrode via a standardized approach in the FOOOF package (Donoghue et al., 2020)
298 (parameters for the fitting: *peak_threshold* = 2, *min_peak_height*: 0.1, *peak_width_limits*: [1, 10],
299 with *max_n_peaks*=2 for the lower range and 0 for the higher one). Fits for every electrode were
300 visually inspected, and any electrodes with clear artifacts on the power spectra, or where the fit
301 was particularly noisy were excluded to ensure an accurate estimation of the spectral exponent.
302 After this step, all remaining electrodes (N= 270) had R² fits of at least 0.8. For our main
303 analyses we were interested in spectral exponents, reported in the main text. The corresponding
304 offsets are reported in Suppl Figure 4-2, for reasons of completeness. Amygdalar electrodes from
305 two patients had a prominent peak in their power spectra around 40 Hz (Figure 4A), which was
306 found for electrodes of the amygdala only, and not other electrodes, and to the best of our
307 knowledge was unrelated to any sources of noise, or pathological findings in these patients. We
308 confirmed that fitting of the spectral exponent was not affected by these peaks in none of the two
309 patients, which were outside the range of our fits.

310 Responsive electrodes

311 Responsive electrodes were identified following common approaches in the field of iEEG
312 (Dürschmid et al., 2016). Briefly, differences between the average signal in post-stimulus time
313 points, $\bar{A}(t)$, and over the entire baseline, \bar{B} , were compared with surrogate distributions
314 computed by random-shifting of the original epochs for $i=1, \dots, 1000$ iterations ($\{A_i(t)-B_i\}_{i=1 \dots 1000}$).
315 Response time points were considered significantly different from the baseline if $\bar{A}(t)-\bar{B}$ fell
316 outside the outer 5% interval of the permuted distribution. Additionally, only electrodes with at
317 least one consecutive response lasting more than 50 ms were kept, to correct for multiple
318 comparisons, as commonly done in the field (Guthrie & Buchwald, 1991; Haller et al., 2018; Kam
319 et al., 2021). The post-stimulus time-points were restricted to the interval [10, 600] ms, to control
320 for too early and too late onsets that would be biologically implausible. We defined the peak
321 latency as the time between the sound onset and the maximum absolute difference voltage from
322 baseline.

323 Statistical analyses

324 Statistical tests have been conducted in R version 4.2.0 (R Development Core Team, 2020) using
325 Linear Mixed-Effects models (LMEs) with a random intercept term corresponding to the patient,
326 to account for the fact that electrodes were recorded from different patients (Yu et al., 2022)
327 (implemented with *nlme* package (Lindstrom & Bates, 1990)). The omnibus tests for the “brain
328 region” factor were computed with F-tests, while post-hoc pairwise comparisons were computed
329 with Tukey’s range test, controlling for multiple comparisons (implemented with *emmeans*
330 package). In the case of omnibus tests on multiple time lags (Fig. 2a) and tests over multiple MNI
331 coordinates, p-values have been Bonferroni-corrected. For regression analyses, we used LMEs
332 with a continuous predictor and a random intercept accounting for across-patient variability. We
333 computed correlation values starting from R^2 as described in (Nakagawa & Schielzeth, 2013) and
334 took the square root, mimicking a fixed-effects-only linear model (implemented with *MuMIn*
335 package (Kamil Barton, 2020)). P-values were computed with F-tests, correcting with Bonferroni
336 when regressing on each level of the region factor separately (p_{corr}).

337 Acknowledgments

338 This work is supported by the Inselspital University Hospital Bern, the Interfaculty Research
339 Cooperation “Decoding Sleep: From Neurons to Health & Mind” of the University of Bern (AA, IB,
340 AT, SLA), the Swiss National Science Foundation (AA, #320030_188737 AT), the European
341 Research Council (CoG-725850 to A.A.), the Synapsis Foundation (AA), the University of Bern
342 (AA), and the Fondation Pierre Mercier pour la science (AT). The authors thank Prof. Johannes
343 Sarnthein for support with recordings and feedback on the manuscript.

344 Data and code availability

345 Because of the sensitive nature of the data, data and code can be made available from the
346 corresponding author upon reasonable request.

347

348 Competing interests

349 MOB holds shares with Epios SA, a medical device company based in Geneva.

350

351 References

352 Alnes, S. L., Lucia, M. D., Rossetti, A. O., & Tzovara, A. (2021). Complementary roles of neural
353 synchrony and complexity for indexing consciousness and chances of surviving in acute
354 coma. *NeuroImage*, 245, 118638. <https://doi.org/10.1016/j.neuroimage.2021.118638>

355 Blenkmann, A. O., Collavini, S., Lubell, J., Llorens, A., Funderud, I., Ivanovic, J., Larsson, P. G.,
356 Meling, T. R., Bekinschtein, T., Kochen, S., Endestad, T., Knight, R. T., & Solbakk, A.-K.
357 (2019). Auditory deviance detection in the human insula: An intracranial EEG study.
358 *Cortex*, 121, 189–200. <https://doi.org/10.1016/j.cortex.2019.09.002>

359 Camalier, C. R., D'Angelo, W. R., Sterbing-D'Angelo, S. J., de la Mothe, L. A., & Hackett, T. A.
360 (2012). Neural latencies across auditory cortex of macaque support a dorsal stream
361 supramodal timing advantage in primates. *Proceedings of the National Academy of*
362 *Sciences*, 109(44), 18168–18173. <https://doi.org/10.1073/pnas.1206387109>

363 Chaudhuri, R., Knoblauch, K., Gariel, M.-A., Kennedy, H., & Wang, X.-J. (2015). A Large-Scale
364 Circuit Mechanism for Hierarchical Dynamical Processing in the Primate Cortex. *Neuron*,
365 88(2), 419–431. <https://doi.org/10.1016/j.neuron.2015.09.008>

366 Donoghue, T., Haller, M., Peterson, E. J., Varma, P., Sebastian, P., Gao, R., Noto, T., Lara, A.
367 H., Wallis, J. D., Knight, R. T., Shestyuk, A., & Voytek, B. (2020). Parameterizing neural
368 power spectra into periodic and aperiodic components. *Nature Neuroscience*, 23(12),
369 1655–1665. <https://doi.org/10.1038/s41593-020-00744-x>

370 Dürschmid, S., Edwards, E., Reichert, C., Dewar, C., Hinrichs, H., Heinze, H.-J., Kirsch, H. E.,

- 371 Dalal, S. S., Deouell, L. Y., & Knight, R. T. (2016). Hierarchy of prediction errors for
372 auditory events in human temporal and frontal cortex. *Proceedings of the National*
373 *Academy of Sciences*, 113(24), 6755–6760. <https://doi.org/10.1073/pnas.1525030113>
- 374 Gao, R., Peterson, E. J., & Voytek, B. (2017). Inferring synaptic excitation/inhibition balance
375 from field potentials. *NeuroImage*, 158, 70–78.
376 <https://doi.org/10.1016/j.neuroimage.2017.06.078>
- 377 Gao, R., van den Brink, R. L., Pfeffer, T., & Voytek, B. (2020). Neuronal timescales are
378 functionally dynamic and shaped by cortical microarchitecture. *ELife*, 9, e61277.
379 <https://doi.org/10.7554/eLife.61277>
- 380 Gerster, M., Waterstraat, G., Litvak, V., Lehnertz, K., Schnitzler, A., Florin, E., Curio, G., &
381 Nikulin, V. (2021). *Separating neural oscillations from aperiodic 1/f activity: Challenges*
382 *and recommendations* (p. 2021.10.15.464483).
383 <https://doi.org/10.1101/2021.10.15.464483>
- 384 Golesorkhi, M., Gomez-Pilar, J., Zilio, F., Berberian, N., Wolff, A., Yagoub, M. C. E., & Northoff,
385 G. (2021). The brain and its time: Intrinsic neural timescales are key for input
386 processing. *Communications Biology*, 4(1), 1–16. [https://doi.org/10.1038/s42003-021-](https://doi.org/10.1038/s42003-021-02483-6)
387 [02483-6](https://doi.org/10.1038/s42003-021-02483-6)
- 388 Gramfort, A., Luessi, M., Larson, E., Engemann, D., Strohmeier, D., Brodbeck, C., Goj, R., Jas,
389 M., Brooks, T., Parkkonen, L., & Hämäläinen, M. (2013). MEG and EEG data analysis
390 with MNE-Python. *Frontiers in Neuroscience*, 7.
391 <https://www.frontiersin.org/articles/10.3389/fnins.2013.00267>
- 392 Guthrie, D., & Buchwald, J. S. (1991). Significance Testing of Difference Potentials.
393 *Psychophysiology*, 28(2), 240–244. <https://doi.org/10.1111/j.1469-8986.1991.tb00417.x>
- 394 Halgren, E., Squires, N. K., Wilson, C. L., Rohrbaugh, J. W., Babb, T. L., & Crandall, P. H.
395 (1980). Endogenous Potentials Generated in the Human Hippocampal Formation and
396 Amygdala by Infrequent Events. *Science*, 210(4471), 803–805.

- 397 <https://doi.org/10.1126/science.7434000>
- 398 Haller, M., Case, J., Crone, N. E., Chang, E. F., King-Stephens, D., Laxer, K. D., Weber, P. B.,
399 Parvizi, J., Knight, R. T., & Shestyuk, A. Y. (2018). Persistent neuronal activity in human
400 prefrontal cortex links perception and action. *Nature Human Behaviour*, 2(1), 80–91.
401 <https://doi.org/10.1038/s41562-017-0267-2>
- 402 Hasson, U., Yang, E., Vallines, I., Heeger, D. J., & Rubin, N. (2008). A Hierarchy of Temporal
403 Receptive Windows in Human Cortex. *Journal of Neuroscience*, 28(10), 2539–2550.
404 <https://doi.org/10.1523/JNEUROSCI.5487-07.2008>
- 405 Honey, C. J., Thesen, T., Donner, T. H., Silbert, L. J., Carlson, C. E., Devinsky, O., Doyle, W.
406 K., Rubin, N., Heeger, D. J., & Hasson, U. (2012). Slow Cortical Dynamics and the
407 Accumulation of Information over Long Timescales. *Neuron*, 76(2), 423–434.
408 <https://doi.org/10.1016/j.neuron.2012.08.011>
- 409 Horn, A., & Kühn, A. A. (2015). Lead-DBS: A toolbox for deep brain stimulation electrode
410 localizations and visualizations. *NeuroImage*, 107, 127–135.
411 <https://doi.org/10.1016/j.neuroimage.2014.12.002>
- 412 Johnson, E. L., Kam, J. W. Y., Tzovara, A., & Knight, R. T. (2020). Insights into human cognition
413 from intracranial EEG: A review of audition, memory, internal cognition, and causality.
414 *Journal of Neural Engineering*, 17(5), 051001. <https://doi.org/10.1088/1741-2552/abb7a5>
- 415 Kam, J. W. Y., Helfrich, R. F., Solbakk, A.-K., Endestad, T., Larsson, P. G., Lin, J. J., & Knight,
416 R. T. (2021). Top–Down Attentional Modulation in Human Frontal Cortex: Differential
417 Engagement during External and Internal Attention. *Cerebral Cortex*, 31(2), 873–883.
418 <https://doi.org/10.1093/cercor/bhaa262>
- 419 Kamil Barton. (2020). *Mu-MIn: Multi-model inference, version 0.12.2/R18*. R Package Version.
420 <http://R-Forge.R-project.org/projects/mumin/>
- 421 Lachaux, J.-P., Axmacher, N., Mormann, F., Halgren, E., & Crone, N. E. (2012). High-frequency
422 neural activity and human cognition: Past, present and possible future of intracranial

- 423 EEG research. *Progress in Neurobiology*, 98(3), 279–301.
- 424 <https://doi.org/10.1016/j.pneurobio.2012.06.008>
- 425 Lendner, J. D., Helfrich, R. F., Mander, B. A., Romundstad, L., Lin, J. J., Walker, M. P., Larsson,
426 P. G., & Knight, R. T. (2020). An electrophysiological marker of arousal level in humans.
427 *ELife*, 9, e55092. <https://doi.org/10.7554/eLife.55092>
- 428 Lindstrom, M. J., & Bates, D. M. (1990). Nonlinear Mixed Effects Models for Repeated
429 Measures Data. *Biometrics*, 46(3), 673–687. <https://doi.org/10.2307/2532087>
- 430 Mercier, M. R., Dubarry, A.-S., Tadel, F., Avanzini, P., Axmacher, N., Cellier, D., Vecchio, M. D.,
431 Hamilton, L. S., Hermes, D., Kahana, M. J., Knight, R. T., Llorens, A., Megevand, P.,
432 Melloni, L., Miller, K. J., Piai, V., Puce, A., Ramsey, N. F., Schwiedrzik, C. M., ...
433 Oostenveld, R. (2022). Advances in human intracranial electroencephalography
434 research, guidelines and good practices. *NeuroImage*, 260, 119438.
435 <https://doi.org/10.1016/j.neuroimage.2022.119438>
- 436 Murray, J. D., Bernacchia, A., Freedman, D. J., Romo, R., Wallis, J. D., Cai, X., Padoa-
437 Schioppa, C., Pasternak, T., Seo, H., Lee, D., & Wang, X.-J. (2014). A hierarchy of
438 intrinsic timescales across primate cortex. *Nature Neuroscience*, 17(12), 1661–1663.
439 <https://doi.org/10.1038/nn.3862>
- 440 Nakagawa, S., & Schielzeth, H. (2013). A general and simple method for obtaining R² from
441 generalized linear mixed-effects models. *Methods in Ecology and Evolution*, 4(2), 133–
442 142. <https://doi.org/10.1111/j.2041-210x.2012.00261.x>
- 443 Nourski, K. V., Steinschneider, M., McMurray, B., Kovach, C. K., Oya, H., Kawasaki, H., &
444 Howard, M. A. (2014). Functional organization of human auditory cortex: Investigation of
445 response latencies through direct recordings. *NeuroImage*, 101, 598–609.
446 <https://doi.org/10.1016/j.neuroimage.2014.07.004>
- 447 R Development Core Team. (2020). *R: A language and environment for statistical computing*. R
448 Foundation for Statistical Computing. <https://www.r-project.org/>

- 449 Raut, R. V., Snyder, A. Z., & Raichle, M. E. (2020). Hierarchical dynamics as a macroscopic
450 organizing principle of the human brain. *Proceedings of the National Academy of*
451 *Sciences*, *117*(34), 20890–20897. <https://doi.org/10.1073/pnas.2003383117>
- 452 Seabold, S., & Perktold, J. (2010). Statsmodels: Econometric and Statistical Modeling with
453 Python. In S. van der Walt & J. Millman (Eds.), *Proceedings of the 9th Python in Science*
454 *Conference* (pp. 92–96). <https://doi.org/10.25080/Majora-92bf1922-011>
- 455 Tzovara, A., Meyer, S. S., Bonaiuto, J. J., Abivardi, A., Dolan, R. J., Barnes, G. R., & Bach, D.
456 R. (2019). High-precision magnetoencephalography for reconstructing amygdalar and
457 hippocampal oscillations during prediction of safety and threat. *Human Brain Mapping*,
458 *40*(14), 4114–4129. <https://doi.org/10.1002/hbm.24689>
- 459 Virtanen, P., Gommers, R., Oliphant, T. E., Haberland, M., Reddy, T., Cournapeau, D.,
460 Burovski, E., Peterson, P., Weckesser, W., Bright, J., van der Walt, S. J., Brett, M.,
461 Wilson, J., Millman, K. J., Mayorov, N., Nelson, A. R. J., Jones, E., Kern, R., Larson, E.,
462 ... van Mulbregt, P. (2020). SciPy 1.0: Fundamental algorithms for scientific computing
463 in Python. *Nature Methods*, *17*(3), 261–272. <https://doi.org/10.1038/s41592-019-0686-2>
- 464 Wang, X.-J. (2020). Macroscopic gradients of synaptic excitation and inhibition in the neocortex.
465 *Nature Reviews Neuroscience*, *21*(3), 169–178. [https://doi.org/10.1038/s41583-020-](https://doi.org/10.1038/s41583-020-0262-x)
466 [0262-x](https://doi.org/10.1038/s41583-020-0262-x)
- 467 Yu, Z., Guindani, M., Grieco, S. F., Chen, L., Holmes, T. C., & Xu, X. (2022). Beyond t test and
468 ANOVA: Applications of mixed-effects models for more rigorous statistical analysis in
469 neuroscience research. *Neuron*, *110*(1), 21–35.
470 <https://doi.org/10.1016/j.neuron.2021.10.030>

471

472

473

474 **Supplementary material**

475 **Supplementary tables**

476

Patient ID	Clinic	# of electrodes analyzed	Hemisphere	Regions
1	Zürich	25	L + R	CTX, ENT, HIP, AMY
2	Bern	17	R	CTX, ENT, HIP
3	Zürich	34	L + R	CTX, ENT, HIP, AMY
4	Zürich	30	L + R	CTX, ENT, HIP, AMY
5	Zürich	28	L + R	CTX, ENT, HIP, AMY
6	Zürich	20	L	CTX, ENT, HIP, AMY
7	Zürich	37	L + R	CTX, ENT, HIP, AMY
8	Bern	24	L	CTX, ENT, HIP
9	Zürich	28	L + R	CTX, ENT, HIP, AMY
10	Zürich	19	R	CTX, ENT, HIP, AMY
11	Bern	8	L	CTX, HIP

477

478 **Supplementary Table 1.** Overview of patients dataset. We collected a total of 270 electrodes
479 from 11 patients, with a median of 25 electrodes per patient and minimum and maximum of 8 and
480 37 electrodes. For each patient, we report the hospital where the data were collected, the # of
481 electrodes used for our analyses, the hemisphere(s) where the electrodes were implanted and
482 the regions sampled from the retained electrodes.

Comparison	t-value	p-value
CTX-ENT	-2.383	0.083
CTX-HIP	-6.099	2.34×10^{-8}
CTX-AMY	-7.716	1.69×10^{-12}
ENT-HIP	-2.817	0.027
ENT-AMY	-4.635	3.36×10^{-5}
HIP-AMY	-2.067	0.167

483
484
485
486
487
488
489
490
491
492

Supplementary Table 2. Pairwise comparisons of intrinsic neural timescales across regions of interest. The first column lists each of the six pairwise comparisons, the second one the t-values of the post-hoc t-test, and the third column the related p-values. All pairs of cortical-limbic areas have significant differences in their intrinsic timescales, while the differences between temporal/entorhinal cortex and hippocampus/amygdala are non-significant. The timescale values are computed through a mixed-effects model with a patient-specific random effect and p-values are corrected for multiple comparisons via the Tuckey range test.

Comparison	t-value	p-value
CTX-ENT	2.557	0.054
CTX-HIP	12.421	4.34×10^{-14}
CTX-AMY	11.409	5.35×10^{-14}
ENT-HIP	7.591	3.63×10^{-12}
ENT-AMY	7.564	4.27×10^{-12}
HIP-AMY	0.608	0.929

493
494
495
496
497
498
499
500

Supplementary Table 3. Pairwise comparisons of 20-35 Hz spectral exponents among the four regions of interest. The first column lists each of the six pairwise comparisons, the second one the t-values of the post-hoc t-test, and the last one the related p-values. All pairs of cortical-limbic areas have significant differences in their 20-35 Hz exponent, while the difference between temporal and entorhinal cortex is slightly above significance threshold. The spectral exponent values are computed through a mixed-effects model with a patient-specific random effect and p-values are corrected for multiple comparisons via the Tuckey range test.

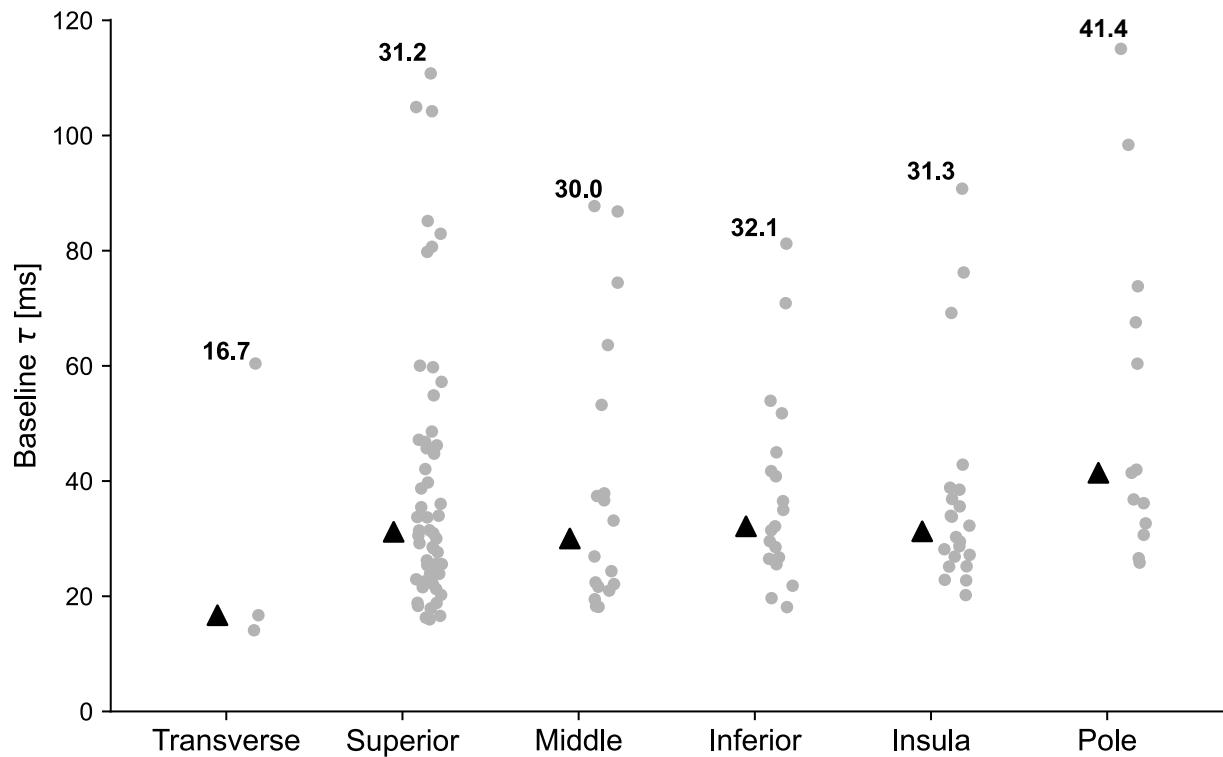
501

Comparison	t-value	p-value
CTX-ENT	1.551	0.408
CTX-HIP	-14.214	4.31×10^{-14}
CTX-AMY	1.631	0.363
ENT-HIP	-12.321	4.35×10^{-14}
ENT-AMY	0.195	0.997
HIP-AMY	11.650	4.90×10^{-14}

502

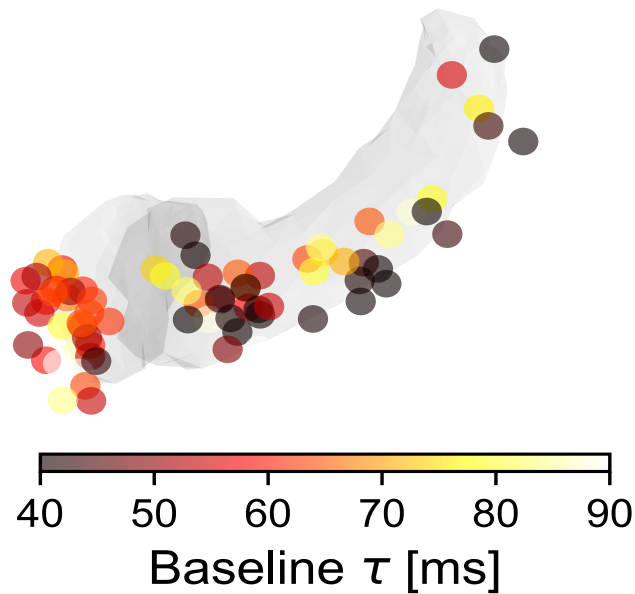
503 **Supplementary Table 4.** Pairwise comparisons of 80-150 Hz spectral exponents among the four
504 regions of interest. The first column lists each of the six pairwise comparisons, the second one
505 the t-values of the post-hoc t-tests, and the last one the related p-values. Only the comparisons
506 between hippocampus and the other areas are significant due to the very steep slope of
507 hippocampal electrodes in the high-gamma range. The spectral exponent values are computed
508 through a mixed-effects model with a patient-specific random effect and p-values are corrected
509 for multiple comparisons via the Tuckey range test.

510 Supplementary figures

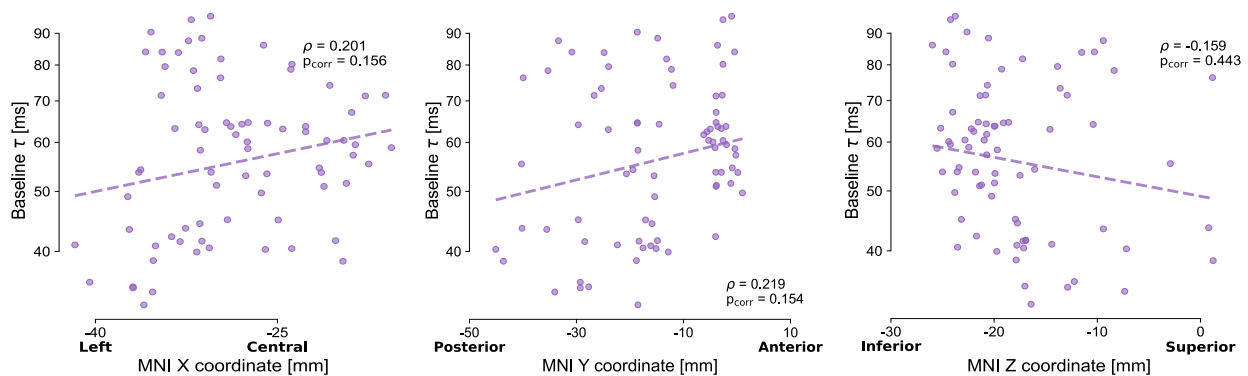


511
512 **Supplementary Figure 2-1. Intrinsic neural timescales across cortical sub-divisions.**
513 Intrinsic neural timescales of cortical electrodes, divided in anatomical subregions. Black triangles
514 indicate median values, while the actual value is written for each region. The fastest timescales
515 are observed for the transverse temporal gyrus, at 16.7 ms. All of the remaining cortical sub-
516 divisions apart from the temporal pole have median timescales around 30-32 ms, with variations
517 within them. The temporal pole by contrast has the longest timescales, with a median of 41.4 ms.
518 The anatomical location of each electrode can be found in Figure 2 of the main text. Transverse:
519 transverse temporal gyrus; Superior: superior temporal gyrus and sulcus; Middle: middle temporal
520 gyrus; Inferior: inferior temporal gyrus and sulcus; Insula: inferior circular sulcus of insula; Pole:
521 temporal pole.

A



B



522

523

524

525

526

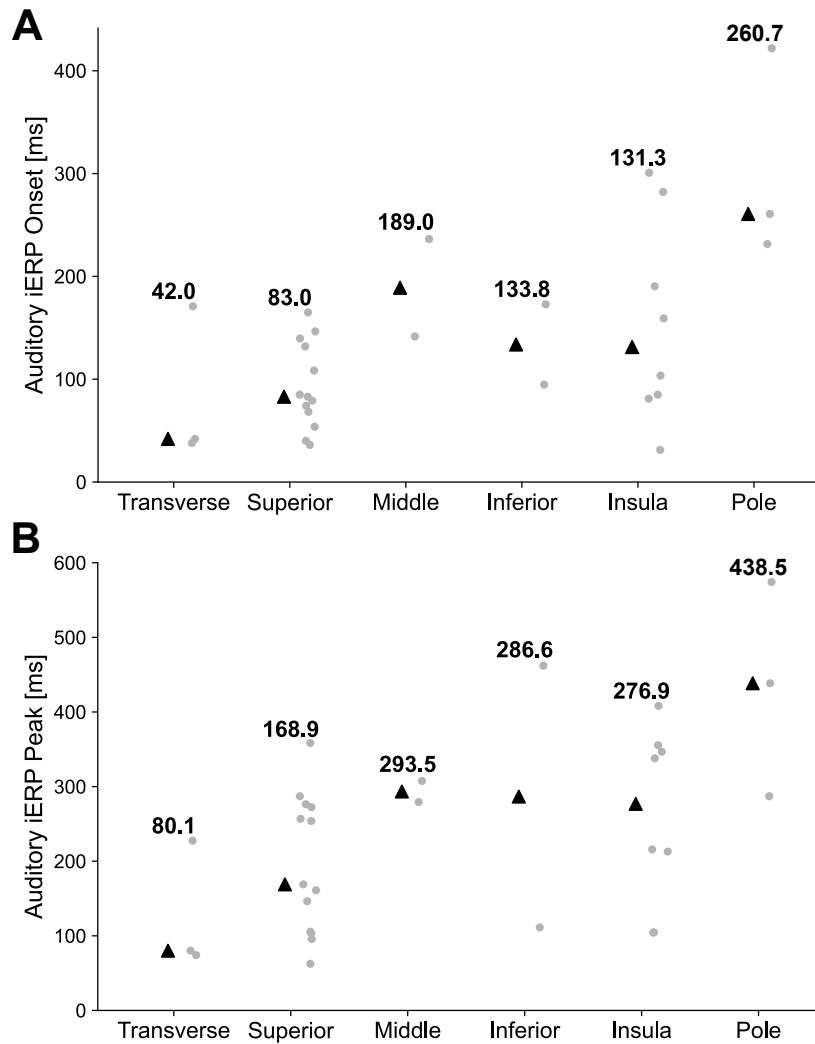
527

528

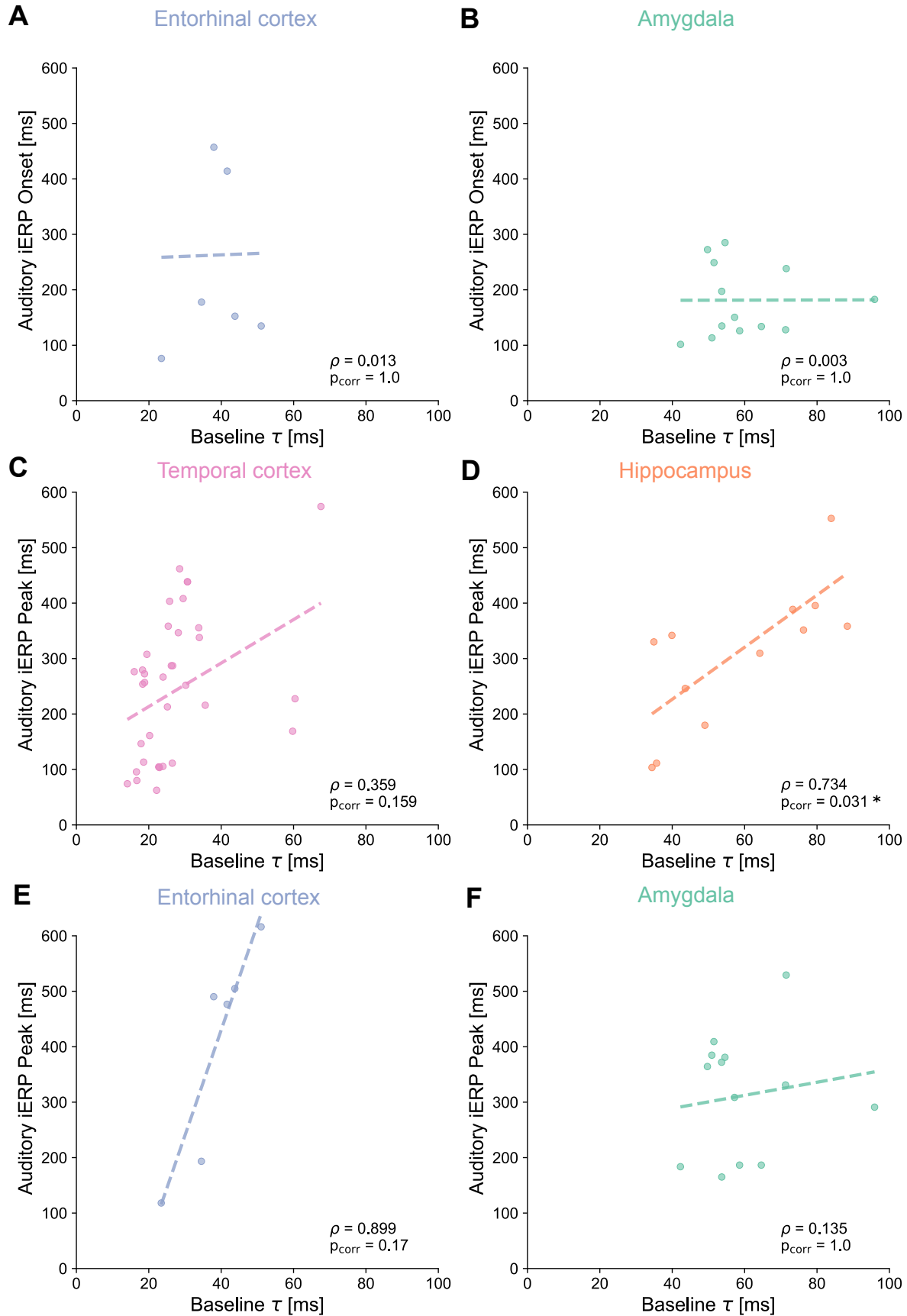
529

530

Supplementary Figure 2-2. Intrinsic neural timescales at rest in the hippocampus and amygdala. A. Anatomical organization of intrinsic timescales throughout the hippocampus and amygdala, with the color map quantifying the intrinsic timescale for each electrode. B. Correlations between MNI coordinates and intrinsic timescale (τ) across electrodes. Although τ tends to be slower for anterior electrodes, and in particular for the amygdala, correlations in the X, Y, and Z directions are not significant ($\rho_x=0.201$, $p_x=0.156$; $\rho_y=0.219$, $p_y=0.154$; $\rho_z=-0.159$, $p_z=0.443$; p-values after Bonferroni correction). For display purposes, all electrodes have been projected to the left hemisphere.

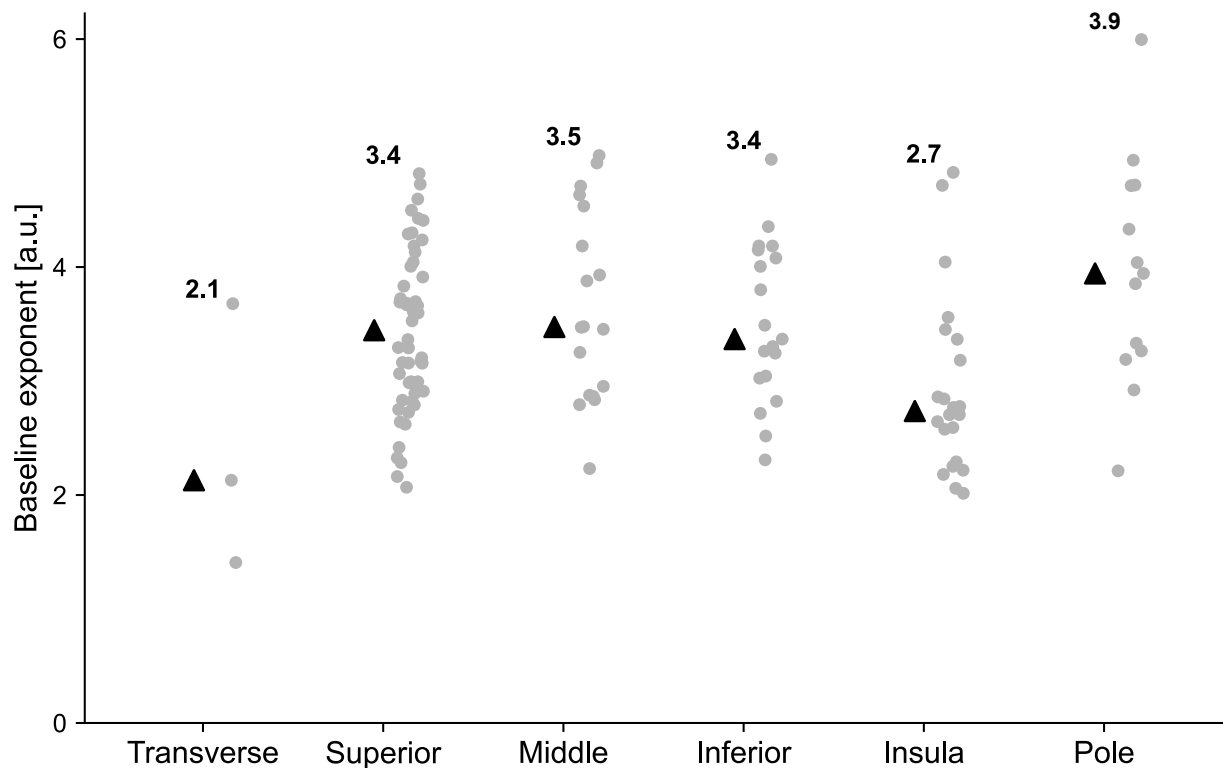


531
532 **Supplementary Figure 3-1. Auditory response latencies across cortical sub-regions.** Onset
533 latency (A) and peak latency (B) of Temporal cortex electrodes, divided by anatomical subregion.
534 Black triangles indicate median values, with the actual value written for each sub-region. The
535 transverse temporal gyrus has the earliest onsets (median at 42.0 ms) and peaks (median at 80.1
536 ms), followed by the superior temporal gyrus/sulcus, at 83 ms for onset and 168.9 ms for peak.
537 The latest responses are observed for the temporal pole, with a median onset at 260.7 ms.
538 Transverse: transverse temporal gyrus; Superior: superior temporal gyrus and sulcus; Middle:
539 middle temporal gyrus; Inferior: inferior temporal gyrus and sulcus; Insula: inferior circular sulcus
540 of insula; Pole: temporal pole.
541

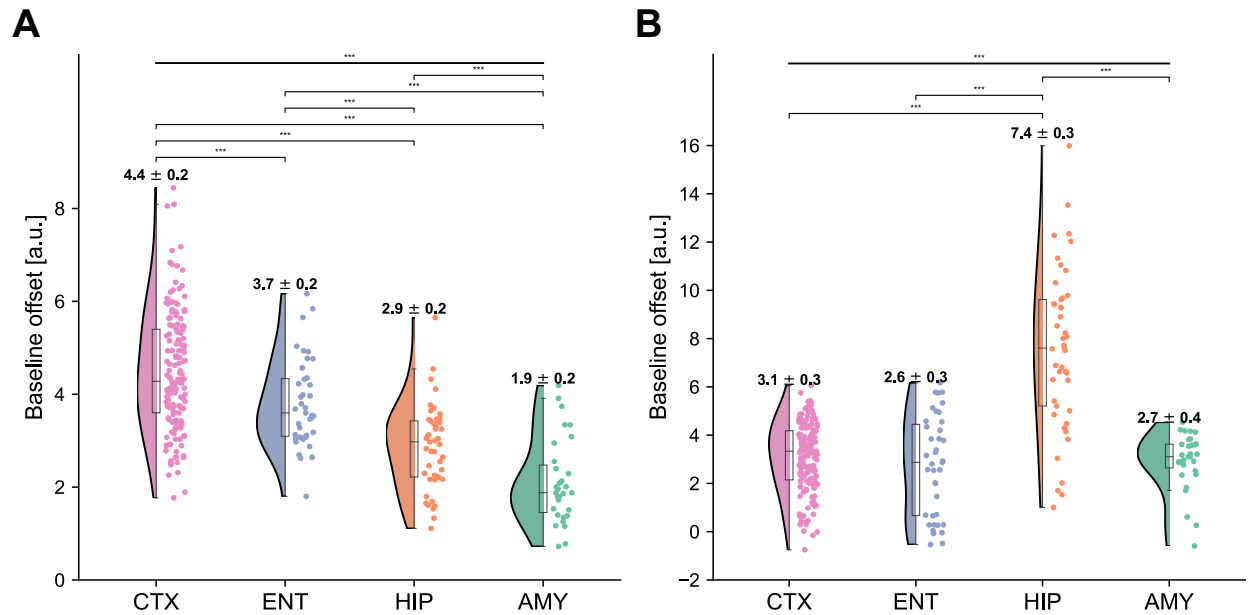


543 **Supplementary Figure 3-2. Relation between onset and peak latencies of auditory**
544 **responses and intrinsic timescales at rest within brain regions.** A, B Intrinsic timescales τ at
545 baseline (x-axis) and onsets of iERPs (y-axis) for entorhinal cortex (A) and amygdala (B) are not
546 correlated. C, D, E, F Intrinsic timescales τ at baseline (x-axis) and peaks of iERPs (y-axis) for
547 temporal cortex (C), hippocampus (D), entorhinal cortex (E), and amygdala (F). Only the
548 regression of intrinsic timescales on iERP peak in the hippocampus is significant. The ranges in
549 both axes are kept constant across panels to facilitate comparison.

550
551
552
553
554



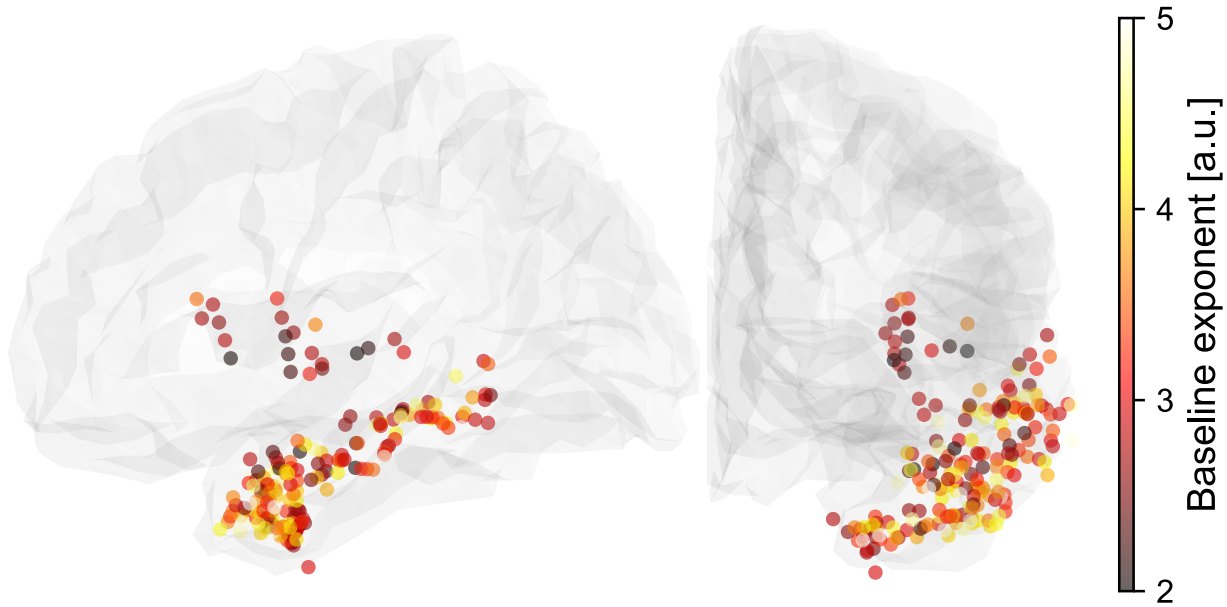
555 **Supplementary Figure 4-1. 20-35 Hz spectral exponent at baseline across cortical sub-**
556 **divisions.** Spectral exponents of cortical electrodes, divided by anatomical subregion. Black
557 triangles indicate median values, along with the actual value written on top. Transverse:
558 transverse temporal gyrus; Superior: superior temporal gyrus and sulcus; Middle: middle temporal
559 gyrus; Inferior: inferior temporal gyrus and sulcus; Insula: inferior circular sulcus of insula; Pole:
560 temporal pole.
561



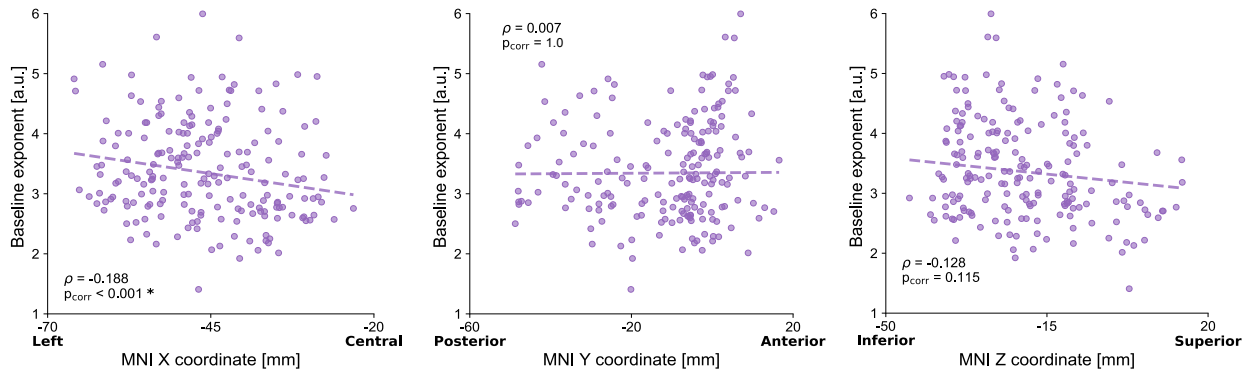
562
563
564
565
566
567
568

Supplementary Figure 4-2. 20-35 Hz spectral offset across brain regions. A. The spectral offset at 20-35 Hz is plotted for each electrode, and shows a significant main effect of region ($F(3,256)=72.995$, $p<10^{-16}$), with the temporal cortex having the highest offset, followed by the entorhinal cortex, hippocampus, and amygdala. B. Spectral offset at 80-150 Hz shows a significant effect of region ($F(3,256)=73.832$, $p<10^{-16}$), with the hippocampus having the highest value. The corresponding exponents can be found in Figure 4, main manuscript.

A



B



569

570 **Supplementary Figure 4-3. 20-35 Hz spectral exponent at rest in cortical electrodes. A.**

571 Anatomical organization of spectral exponent throughout the temporal and entorhinal cortices,

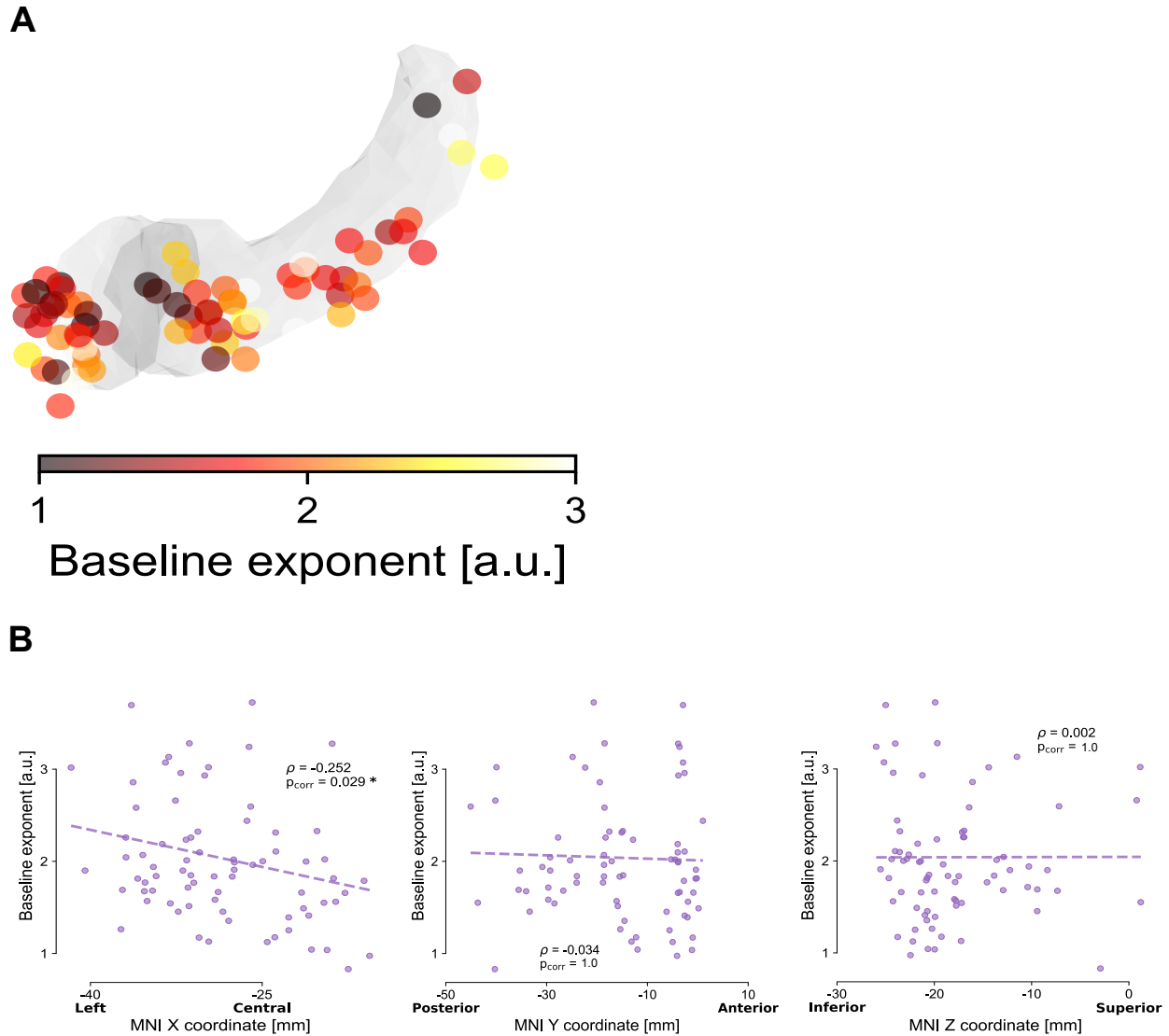
572 with the color map quantifying the exponent for each electrode. B. Correlations between MNI

573 coordinates and spectral exponent across electrodes show significance for the X (medio-lateral)

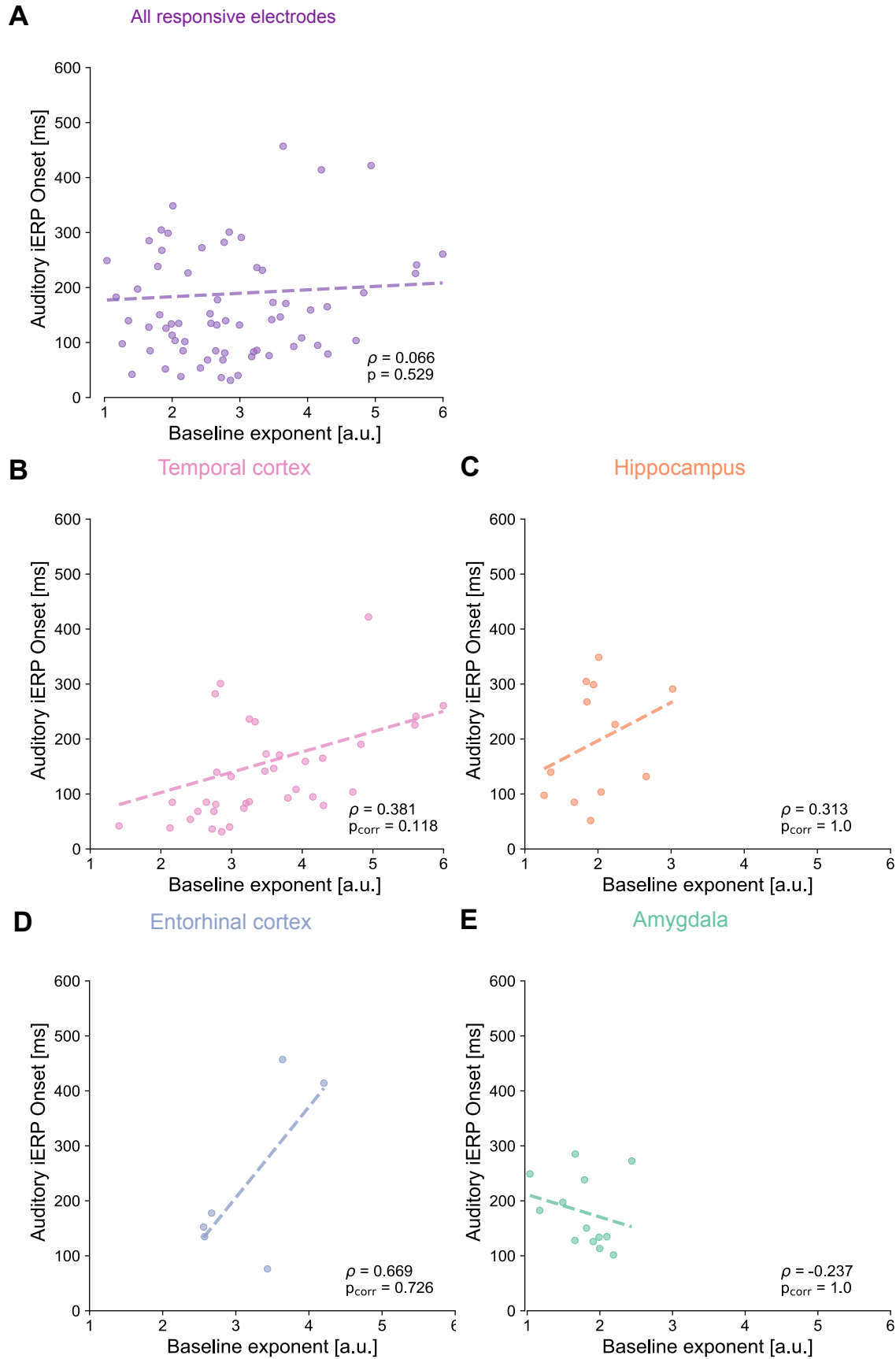
574 and Z (inferior-superior) directions ($\rho_x = -0.188$, $p_x = 9.988 \times 10^{-4}$; $\rho_y = 0.007$, $p_y = 1.0$; $\rho_z = -0.128$,

575 $p_z = 0.115$; p-values after Bonferroni correction). For display purposes, all electrodes have been

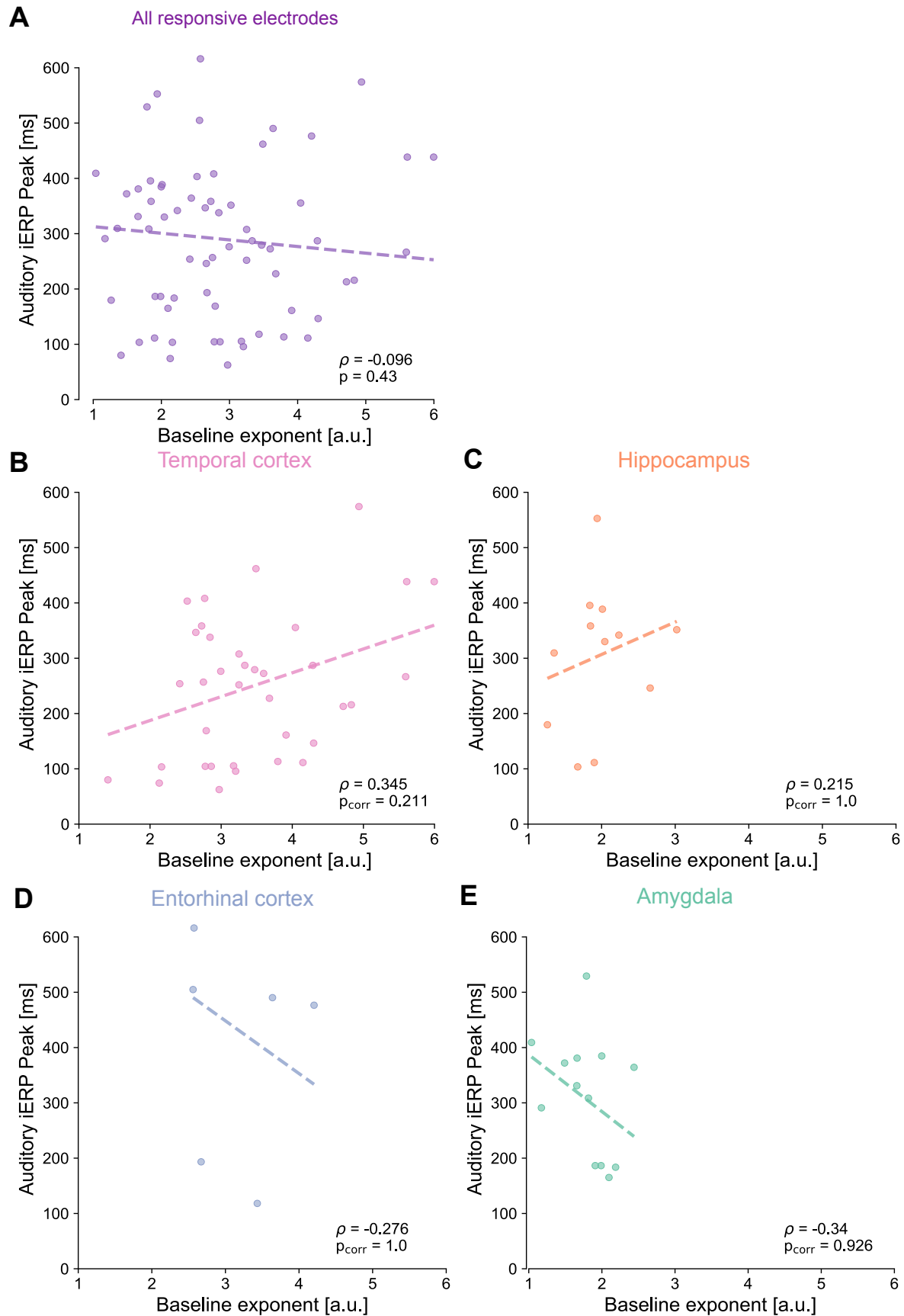
576 projected to the left hemisphere.



577
578 **Supplementary Figure 4-4. 20-35 Hz spectral exponent at rest in hippocampus and**
579 **amygdala.** A. Anatomical organization of spectral exponent throughout the hippocampus and
580 amygdala, with the color map quantifying the exponent for each electrode. B. Correlations
581 between MNI coordinates and spectral exponent for each electrode show significance only for the
582 X (left-central) direction ($\rho_X = -0.252$, $p_X = 0.029$; $\rho_Y = -0.034$, $p_Y = 1.0$; $\rho_Z = 0.002$, $p_Z = 1.0$; p-values after
583 Bonferroni correction). For display purposes, all electrodes have been projected to the left
584 hemisphere.



586 **Supplementary Figure 4-5. Relation between onset latency of auditory responses and 20-**
587 **35 Hz spectral exponent at rest.** Regression of spectral exponent at baseline (x-axis) on onsets
588 of iERPs (y-axis) for all responsive electrodes (A), temporal cortex (B), hippocampus (C),
589 entorhinal cortex (D), and amygdala (E). None of the regression is significant. The reported p
590 values have been corrected for multiple comparisons across regions. Notice the ranges in both
591 axes are kept constant.



593 **Supplementary Figure 4-6. Relation between peak latency of auditory responses and 20-**
594 **35 Hz spectral exponent at rest.** Regression of spectral exponent at baseline (x-axis) on peaks
595 of iERPs (y-axis) for all responsive electrodes (A), temporal cortex (B), hippocampus (C),
596 entorhinal cortex (D), and amygdala (E). None of the regression is significant; all reported p values
597 have been corrected for multiple comparisons. Notice the ranges in both axes are kept constant.